

arXiv:astro-ph/0309037v1 1 Sep 2003
Disks and Halos in Pre-Main-Sequence Stars

By: Dejan Vinković,¹ Željko Ivezić,² Anatoly S. Miroshnichenko³ and Moshe Elitzur¹

¹*Department of Physics & Astronomy, University of Kentucky, Lexington, KY 40506, USA; dejan@pa.uky.edu, moshe@uky.edu*

²*Department of Astrophysical Sciences, Princeton University, Princeton, NJ 08544, USA; ivezic@astro.Princeton.edu; H.N. Russel Fellow*

³*Department of Physics & Astronomy, University of Toledo, Toledo, OH 43606, USA; anatoly@physics.utoledo.edu*

Mon. Not. R. Astron. Soc. **000**, 1–11 (2003) Printed 2 February 2008 (MN LATEX style file v2.2)

Submitted September 16, 2002; revised August 19, 2003; accepted August 25, 2003

ABSTRACT:

We study the IR emission from flared disks with and without additional optically thin halos. Flux calculations of a flared disk in vacuum can be considered a special case of the more general family of models in which the disk is imbedded in an optically thin halo. In the absence of such halo, flux measurements can never rule out its existence because the disk flaring surface defines a mathematically equivalent halo that produces the exact same flux at all IR wavelengths. When a flared disk with height H at its outer radius R is imbedded in a halo whose optical depth at visual wavelengths is τ_{halo} , the system IR flux is dominated by the halo whenever $\tau_{\text{halo}} > \frac{1}{4} H/R$. Even when its optical depth is much smaller, the halo can still have a significant effect on the disk temperature profile. Imaging is the only way to rule out the existence of a potential halo, and we identify a decisive test that extracts a signature unique to flared disks from imaging observations.

Key words: circumstellar matter — dust — infrared: stars — radiative transfer — stars: imaging— stars: formation—stars: pre-main-sequence

1 INTRODUCTION

Modeling the IR radiation of pre-main-sequence stars has traditionally involved “classic” geometrically-thin optically-thick disks. This approach fails to produce many features of observed spectral energy distributions (SED) in both T Tauri stars (TTS) and Herbig Ae/Be stars (Haebes). One way out of this problem is to supplement the disk emission with a surrounding optically thin halo (e.g. Butner, Natta & Evans 1994; Miroshnichenko et al 1999, MIVE hereafter). A simpler alternative was proposed by Chiang & Goldreich (1997, CG hereafter): The surface skin of any optically thick object is of course optically thin. The emission from the disk surface layer can become significant under certain flaring conditions, and CG present SED fits of a number of TTS purely in terms of flared disks. This proposal was extended to SED modeling of Haebes by Chiang et al (2001) and Natta et al (2001).

While the CG model successfully solves the SED problem with a simple physical explanation, recent high-resolution imaging observations of both TTS and Haebes reveal the presence of halos, ignored in the CG approach. Most striking is the case of GM Aur, a classical TTS whose SED modeling was presented as evidence of the success of the CG approach (Chiang & Goldreich 1999). Indeed, HST/NICMOS images by Schneider et al (2003) show a flared disk with radius of ~ 300 AU, but they also reveal the presence of a surrounding tenuous envelope extending to a radius of ~ 1000 AU. Using detailed Monte Carlo calculations, Schneider et al find that simplified models with flared disk without an imbedding halo fail to replicate the scattered light intensity pattern seen in the NICMOS images. The addition of a halo is essential for successful modeling of both the SED and the images.

Similarly, HST and ground-based imaging by Stapelfeldt et al (2003) of the TTS

HV Tau C show a nearly edge-on flared disk imbedded in a more extended nebulosity. From detailed model calculations Stapelfeldt et al find that although it is possible to fit the SED purely with a flared disk, the flaring is unreasonably large and such models do not reproduce the image adequately. They conclude that a flared disk alone is an inadequate model and that an additional, extended component to the circumstellar density distribution is needed to explain the observations. Finally, from detailed modeling of flared disk SED Kikuchi, Nakamoto & Ogochi (2002) conclude that halos are necessary supplements in explaining flat-spectrum TTS.

High resolution observations of Haebes give similar evidence for imbedding halos. Combining space- and ground-based observations of HD 100546, the nearest Herbig Be star, Grady et al (2001) resolve the disk, which extends to $5''$ (~ 500 AU) from the star and displays the elongation of inclined viewing with $i = 49^\circ$. But they also find that the disk is imbedded in a more extended halo ($\sim 10''$ radius) that is roughly circular in shape and optically thin (background stars are visible through it). Polonski et al (2002) performed high-resolution ground-based observations of a sample of Haebes whose mid-IR emission was claimed to be disk-dominated by Hillenbrand et al (1992). They find instead that the emission is not confined to an optically thick disk but originates in a more complex environment that includes large, extended dust envelopes. From analysis of ISO data, Creech-Eakman et al (2002) conclude that only a subset of the Haebes they observe can be described purely in terms of the CG model (notably, E.I. Chiang is a coauthor of this study).

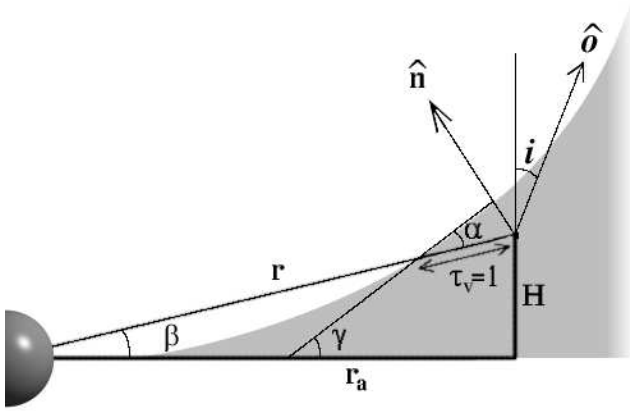


Figure 1. Model geometry and notations for a flared disk and its CG surface layer. The unit vector \hat{o} points at the observer's direction.

How can the SED of the same T-Tauri star, GM Aur, be fitted successfully with a flared disk both with a halo (Schneider et al 2003) and without one (Chiang & Goldreich 1999)? Is it at all possible to distinguish between these two cases? What, if any, is the unique radiative signature of each component? Obviously, imbedding a disk in a tenuous halo with a very small optical depth is not going to affect its emission appreciably. At which stage then does the halo assume a significant role? Here we address these questions. In appendix A we derive general results for the emission from optically thin dust in an arbitrary geometry. We apply these results to the surface layers of flared disks in §2 and to halos in which the disks could be imbedded in §3.

2 FLARED DISKS

2.1 The CG layer and its equivalence to spherical halo

Chiang and Goldreich (1997) noted that the emission from the optically thin surface layer of an optically thick disk, which has been neglected traditionally, can become significant under certain flaring conditions. The stellar radiation penetrates to an optical distance $\tau_V = 1$ along a direction slanted to the surface by angle α (figure 1). The optical depth of the corresponding skin layer along the normal to the surface \hat{n} is α at visual and αq_ν at wavelength ν , where $q_\nu = \sigma_\nu / \sigma_V$ and σ_V is the dust cross-section at visual. In the case of a flat thin disk whose inner radius is determined by dust sublimation, the grazing angle is

$$\alpha_{\text{flat}} = \frac{\alpha^*}{a}, \quad \text{where} \quad \alpha^* = \frac{4 R_*}{3\pi R_s}, \quad a = \frac{r_a}{R_s}; \quad (1)$$

here R_* is the radius of the star, R_s is the dust sublimation radius (eq. A1) and r_a is distance from the axis. Flaring is defined by the radial profile of the disk height H ($\ll r_a$) or, equivalently,

$$\beta = \arctan \frac{H}{r_a} \simeq \frac{H}{r_a}. \quad (2)$$

As is evident from figure 1, $\alpha = \gamma - \beta$ where $\tan \gamma = dH/dr_a$, therefore the grazing angle of a flared disk is

$$\alpha = a \frac{d\beta}{da}. \quad (3)$$

The CG surface layer serves as an effective optically thin disk atop the underlying optically thick disk core, and its flux is obtained from the volume integration listed in equation A7. In the

case of face-on orientation, the optical depth of the CG layer obeys $\sigma_\nu \int n_d dz = q_\nu \alpha$, therefore its flux at distance D is

$$F_{\text{CG},\nu} = \frac{2\pi R_s^2}{D^2} q_\nu \int B_\nu(T) \alpha da. \quad (4)$$

Since the temperature profile of optically thin dust depends only on distance from the radiation source, the geometry dependence of this expression enters only from the radial variation of the grazing angle α (reflecting the dust column variation). But other geometries can produce an identical expression. For example, in the case of spherical geometry the flux is controlled by the dimensionless density profile η (equation A8) and the radial optical depth is $\tau_\nu = \sigma_\nu \int n_d dr$. Denoting the optical depth at visual wavelengths by τ_V , the flux is

$$F_{\text{sph},\nu} = \frac{4\pi R_s^2}{D^2} q_\nu \tau_V \int B_\nu(T) \eta y^2 dy, \quad (5)$$

where $y = r/R_s$. Since y and a enter only as integration variables in the last two integrals, the two expressions are mathematically identical if

$$\eta \propto \frac{\alpha(y)}{y} \quad \text{and} \quad \tau_V = \frac{1}{2} \int \alpha \frac{da}{a}. \quad (6)$$

A minor point is that T in eq. 4 is strictly a function of $y = a\sqrt{1+\beta^2}$ rather than a (since temperature is controlled by distance from the star); this slight difference can be ignored because $\beta \ll 1$ everywhere in the disk.

Scattering can be treated similarly and produces the same result since the only difference is that $B_\nu(T)$ is replaced by $J_\nu = L_\nu/4\pi r^2$, another function of y (see equation A3). Therefore, *there is a complete equivalence between spherical halos and the CG surface layers of flared disks*; either case defines a model with the other geometry and the exact same flux. Specifically, equations 1 and 6 show that a thin flat disk is equivalent to a spherical halo with $\eta \propto 1/y^2$ and $\tau_V = \frac{1}{2}\alpha^*$. In the case of a flared disk, equations 3 and 6 show that the CG layer will produce precisely the same flux as a spherical halo with

$$\eta \propto \frac{d\beta}{dy}, \quad \tau_V = \frac{1}{2} [\beta(R_d) - \beta(R_s)]; \quad (7)$$

in particular, the equivalent halo of a disk with flaring angle $\beta \propto 1/a^p$ has density distribution $\eta \propto 1/y^{p+1}$. And conversely—given a spherical halo, the flared disk with the same outer radius and

$$\beta(a) = \beta(1) + 2\tau_V \int_1^a \eta(y) dy \quad (8)$$

will produce the exact same flux from its CG-surface layer.

Each disk defines a mathematically equivalent halo. Although this equivalence was derived only for face-on viewing of the disk, it carries to most inclination angles since the flux from optically thin dust involves a volume integration (equation A7) and the observed fraction of the disk surface layer remains largely intact as long as internal occultation is not too significant. Similarly, the general analysis presented in appendix A shows that the spherical idealization is not essential for the halo geometry. The dust distribution can be flattened and even distorted into irregular shape before severely affecting the emerging flux.

These results resolve the paradox of successful SED fits for the same star, GM Aur, with a flared disk both with a halo (Schneider et al 2003) and without one (Chiang & Goldreich 1999). The halo contribution to the flux can be absorbed into the disk component by readjusting the flaring law, enabling a successful SED fit without a

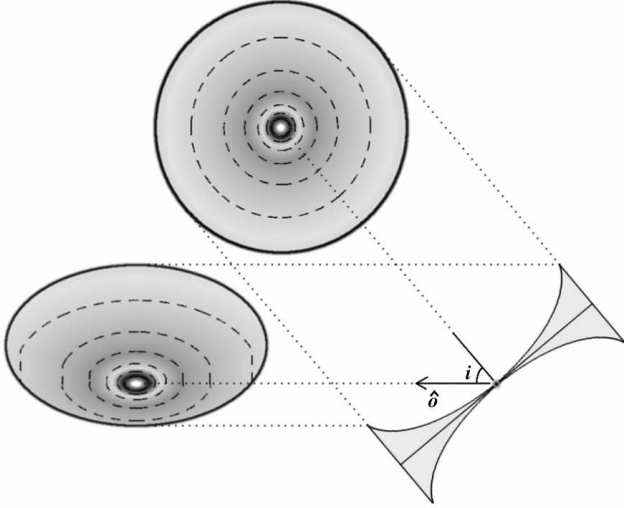


Figure 2. Points on the surface of a flared disk at equal distance from the star lie on a circle centered on the disk axis. The circle retains its shape in pole-on viewing but is deformed into an off-center ellipse (equation 11) in viewing from inclination angle i .

halo even though it is directly visible in imaging observations. The problems Stapelfeldt et al (2003) report with disk-only models of HV Tau C find a similar explanation. The halo contribution to the SED can be shifted to the disk, with the halo optical depth added to the flaring angle (equation 7). This leads to unreasonably large flaring, as Stapelfeldt et al find. The same problem was encountered by Kikuchi et al (2002) in modeling flat-spectrum TTS. The halo optical depth in these sources are sufficiently high that they cannot be substituted by disks with realistic flaring.

In addition to explaining the shortcomings of disk-only models in these specific cases, the equivalence between halos and CG layers has two important broad consequences:

(i) *When the disk is imbedded in a halo that radiates more than its CG layer, the halo becomes the dominant component of the IR flux.* This happens when the halo contains more dust than the halo-equivalent of the disk. From equations 2 and 7, the IR radiation from the system is dominated by the halo contribution whenever

$$\tau_{\text{halo}} > \frac{1}{4} \frac{H(R_d)}{R_d} \quad (9)$$

where τ_{halo} is the optical depth across the halo at visual wavelengths ($2\tau_V$ for spherical halos).

(ii) *It is impossible to distinguish the CG layer of a flared disk from a halo with flux measurements.* Only imaging can produce an unambiguous signature of the CG layer.

2.2 Images

The brightness contours of face-on flared disks are concentric circles centered on the star. Inclined viewing changes the contours substantially. Consider the intensity of radiation scattered from the CG surface layer. It obeys

$$I \propto \frac{\tau(\hat{o})}{r^2} \quad (10)$$

where r is the distance to the star and $\tau(\hat{o})$ the optical depth toward the observer at the scattering point (equation A2). Both factors introduce distinct image asymmetries.

The fundamental reason for image distortion by inclination is that the same projected distance from the star corresponds to widely different locations on the surface of the disk. On that surface, contours of equal distance from the star are circles of radius r_a . When viewed face-on from distance D , each contour appears as a concentric circle of radius $\theta_a = r_a/D$, as seen in the top image in figure 2. At inclination viewing angle i to the disk axis, the contour is no longer circular. Absent flaring, the contour becomes an ellipse centered on the star with major axis $2\theta_a$ and minor axis $2\theta_a \cos i$, aligned with the projection of the disk axis on the plane of the sky. Flaring raises the contour to height $H = r_a \tan \beta$ above the equatorial plane (figure 1), and the star is shifted toward the observer along the minor axis by $\theta_a \tan \beta \sin i$. A point on the contour at position angle ϕ from the near side of the minor axis is observed at displacement $\theta = \theta_a g(\phi)$ from the star, where

$$g(\phi) = [(\tan \beta \sin i - \cos i \cos \phi)^2 + \sin^2 \phi]^{1/2}. \quad (11)$$

These contours are shown in the bottom image of figure 2. The off-center position of the star on the minor axis creates an asymmetry such that the far and near portions of this axis obey $\theta_{\text{far}}/\theta_{\text{near}} = \cos(i - \beta)/\cos(i + \beta)$. Because β increases with θ_a , this asymmetry increases with distance from the star.

At observed displacement (θ, ϕ) from the star, a point on the surface of the disk is located at $r \simeq r_a = D\theta/g(\phi)$. At that point the optical depth of the CG layer toward the observer is $\tau(\hat{o}) = q_\nu \alpha/o(\phi)$, where

$$o(\phi) = \hat{n} \cdot \hat{o} = \cos i \cos \gamma - \sin i \sin \gamma \cos \phi. \quad (12)$$

Therefore the scattering image obeys

$$I(\theta, \phi) \propto \left(\frac{g(\phi)}{\theta} \right)^2 \frac{\alpha}{o(\phi)}. \quad (13)$$

In this expression, both α and γ are determined at the location $r_a = D\theta/g(\phi)$ on the disk surface. A power-law grazing angle $\alpha \propto 1/r_a^p$ produces the image $I(\theta, \phi) \propto [g(\phi)/\theta]^{2+p}/o(\phi)$. This expression and the resulting brightness contours explain the results of Monte Carlo scattering calculations for flared disks (Whitney & Hartmann 1992, Wood et al 1998). Figure 3 shows the scattering images at three viewing angles of a flared disk with the parameters suggested for AB Aur by Dullemond et al (2001).

The images produced at emission wavelengths are handled in complete analogy. The only change is the replacement of r^{-2} by the temperature T , i.e., another function of r , modifying the dependence of brightness on $g(\phi)/\theta$.

2.2.1 Image asymmetry

Brightness contours not subject to rim occultation are ellipses with eccentricity $e = \cos i$ that directly determines the inclination angle irrespective of the flaring profile. The images shown in figure 3 possess an additional deviation from circular symmetry, unique to flaring and conveniently measured by the brightness at diametric locations across an axis through the star

$$A(\theta, \phi) = \frac{I(\theta, \phi + \pi) - I(\theta, \phi)}{I(\theta, \phi + \pi) + I(\theta, \phi)}. \quad (14)$$

This asymmetry parameter vanishes for flat disks at all inclination angles, and for pole-on and edge-on viewing irrespective of the flaring. However, at intermediate inclination angles, flaring introduces substantial asymmetry, as is evident from figure 3.

Non-vanishing A is the hallmark of inclined flared disks because it measures the displacement of the isophote centers from the

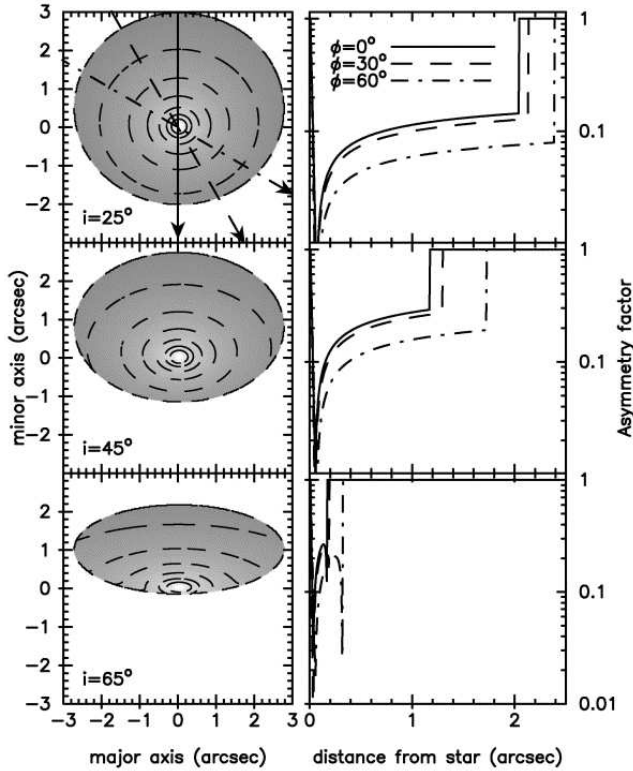


Figure 3. Viewing at inclination angles $i = 25^\circ$, 45° and 65° of radiation scattered off the surface of a flared disk with $3''$ radius and constant grazing angle $\alpha = 4.9^\circ$. For each i , the left panel shows the image with brightness contours, the right panel the asymmetry factor A (equation 14) along three azimuthal directions, shown in the top left panel, whose angles are designated from the observer’s direction. The asymmetry parameter vanishes along the major axis ($\phi = 90^\circ$) at all inclination angles and along any axis at $i = 0^\circ$ and 90° . For flat disks, A is identically zero at all inclination angles.

peak brightness position. Its systematic variation with azimuthal angle easily distinguishes it from deviations from the perfect geometry of idealized models or noise in the data. Each flaring profile produces its own characteristic signature A . For example, it is easy to show that the constant grazing angle α used in figure 3 gives $A \simeq \tan \beta \tan i$ along the minor axis. Therefore, measuring A determines the flaring profile once the inclination is determined from the eccentricity of the brightness contours.

3 HALO-IMBEDDED-DISKS

The results of the previous section show that flux calculations of a flared disk in vacuum can be considered a special case of the more general family of models in which the disk is imbedded in an optically thin halo. In the CG case the “halo” is the disk surface layer, fully determined from the flaring geometry. This layer provides the same IR emission and heating of the underlying optically thick core as its equivalent halo. Therefore, a study of the general halo-imbedded-disk problem contains every possible CG model of flared disks while also covering all cases in which the disk is indeed imbedded in a dusty halo whose optical depth exceeds the bound in equation 9.

Consider a star surrounded by a geometrically thin passive disk and a dusty halo (figure 4). We study the case of a flat disk and a spherical halo, simplifications that enable us to derive analytical

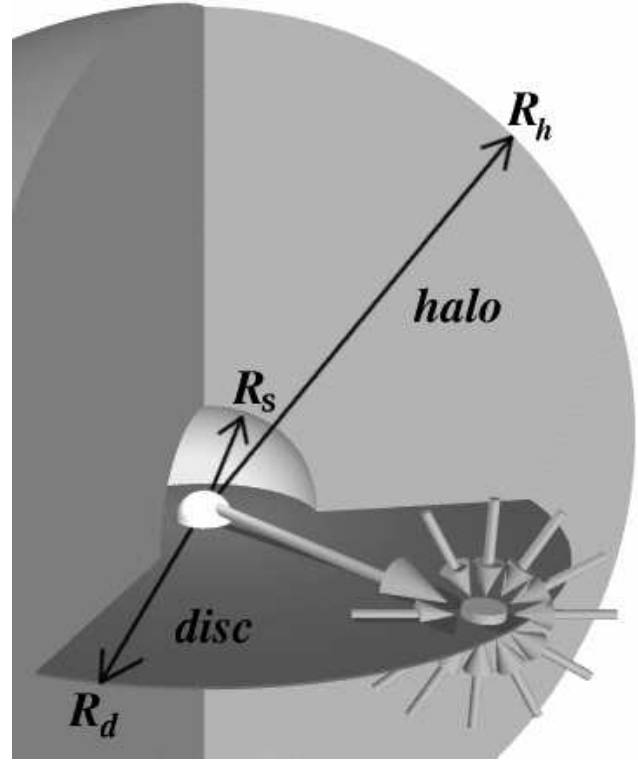


Figure 4. Geometry of the halo-imbedded-disk model: a flat geometrically-thin optically-thick disk extends from the stellar surface to radius R_d . An optically thin spherical halo extends from the dust sublimation radius R_s to R_h . The small pillbox at the disk surface serves as a Gaussian surface for flux conservation.

results and broad conclusions that offer important insight. These simplifications do not cause any serious limitations. As noted previously, the halo geometry can be distorted considerably without much impact on the outcome. And because only the optically thick core of the disk enters into considerations, its only relevant property is its temperature distribution, the surface shape is immaterial. Indeed, Wolf et al (2003) present detailed model calculation of a flared disk imbedded in an envelope pinched around the equatorial plane, and their results fully conform to our conclusions.

The halo extends from the inner radius R_s to some outer radius $R_h = Y R_s$. Thanks to scaling, instead of these radii we can specify the dust temperature on each boundary (see appendix A). The halo is fully characterized by its density profile $\eta(y)$ (eq. A8) and optical depth τ_ν ; only $\tau_\nu \lesssim 1$ is relevant in TTS and Haebeles since the star is always visible. Because of its potentially large optical depth, the disk can extend inside the dust-free cavity where its optical depth comes from the gaseous component. The geometrically-thin disk assumption implies that the disk temperature varies only with radius, vertical temperature structure is ignored. This temperature is calculated from radiative flux conservation through the Gaussian surface in the shape of a small pillbox shown in figure 4. Denote by \mathcal{H} the radiative flux entering the pillbox from above, including both the stellar and diffuse components. Then

$$\sigma T^4 - 2\pi \int B_\nu(T) E_3(\tau_\nu^D) d\nu + \int_{2\pi} \mu I_\nu e^{-\tau_\nu^D/\mu} d\Omega d\nu = \mathcal{H}, \quad (15)$$

where E_3 is the 3rd exponential integral, τ_ν^D is the disk vertical optical depth and μ is the cosine of the angle from the disk nor-

mal. The first two term on the left are the disk contribution to the upward flux, the third is the contribution of local intensity transmitted upward through the disk. When the disk is optically thick at frequencies around the peak of $B_\nu(T)$ ($\tau_\nu^D \gg 1$ for $\nu \sim kT/h$), the second and third terms can be neglected, leading to the standard expression for disk temperature (e.g. Friedjung 1985, Kenyon & Hartmann 1987). We assume this to be the case everywhere in the disk, an assumption that we check for self-consistency in all our model calculations.

With its temperature derived, the disk emission is calculated from $B_\nu(T)[1 - \exp(-\tau_\nu^D/\mu)]$. Because the disk is optically thick around the Planckian peak at all radii, the self-absorption factor can be neglected in the calculation of the disk overall bolometric flux. Then $F_{\text{disk}}(D, i)$, the disk flux observed at distance D and inclination i , is proportional to $\cos i$, reflecting the variation of projected area. This proportionality remains largely unaffected by the envelope attenuation because the short wavelengths, the main contributors to the bolometric flux, emanate from close to the star so that their pathlength is approximately isotropic. Denote by L_{disk} the disk contribution to the overall luminosity L and by L_{sph} the contribution of the (halo + attenuated stellar) spherical component. The corresponding flux components are then

$$F_{\text{disk}}(D, i) = \frac{L_{\text{disk}}}{2\pi D^2} \cos i, \quad F_{\text{sph}}(D) = \frac{L_{\text{sph}}}{4\pi D^2} \quad (16)$$

and the overall flux is

$$F(D, i) = F_{\text{disk}}(D, 0) \cos i + F_{\text{sph}}(D) = \frac{L}{4\pi D^2} \cdot \frac{1 + 2x \cos i}{1 + x}$$

where $x = L_{\text{disk}}/L_{\text{sph}}$. The standard ‘‘bare’’ disk has $L_{\text{disk}} = \frac{1}{4}L$ (Kenyon & Hartmann 1987), therefore in this case $x = \frac{1}{3}$. Larger fractions can occur when the disk is imbedded in a halo because of the heating effect of the diffuse radiation, discussed below.

We performed detailed model calculations with the code DUSTY (Ivezić, Nenkova & Elitzur 1999) which takes into account the energy exchange between the star, halo and disk, including dust scattering, absorption and emission. Because its optical depth is typically $\tau_V \lesssim 1$, the halo is transparent to the disk emission in all the models we consider and we neglect the disk effect on the halo. In all the calculations, the spectral shapes q_ν of the grain absorption and scattering coefficients are those of standard interstellar mix, the sublimation temperature $T_s = 1500$ K. The spectral shape of the stellar radiation is taken from the appropriate Kurucz (1994) model atmosphere.

3.1 Temperature Profiles

The heating rate of a thin flat disk by the stellar radiation at $r \gg R_*$ is

$$\mathcal{H}_* = \frac{2F_s}{3\pi} \frac{R_*}{R_s} \frac{1}{a^3}, \quad (17)$$

where F_s is the stellar flux at R_s and $a = r_a/R_s$, with r_a distance from the axis (Friedjung 1985). This result reflects the $1/a^2$ decline of the stellar solid angle and the $1/a$ variation of the grazing angle, yielding disk temperature variation $T \propto a^{-3/4}$. Natta (1993) noted that imbedding the disk in a dusty halo can significantly affect its temperature even at small halo optical depths (see also D’Alessio, Calvet & Hartmann 1997 for the effect of optically thick halos). With a simple model for scattering at a single wavelength she found that the disk temperature law becomes $T \propto a^{-(1+p)/4}$ if the halo density profile is $\eta \propto y^{-p}$.

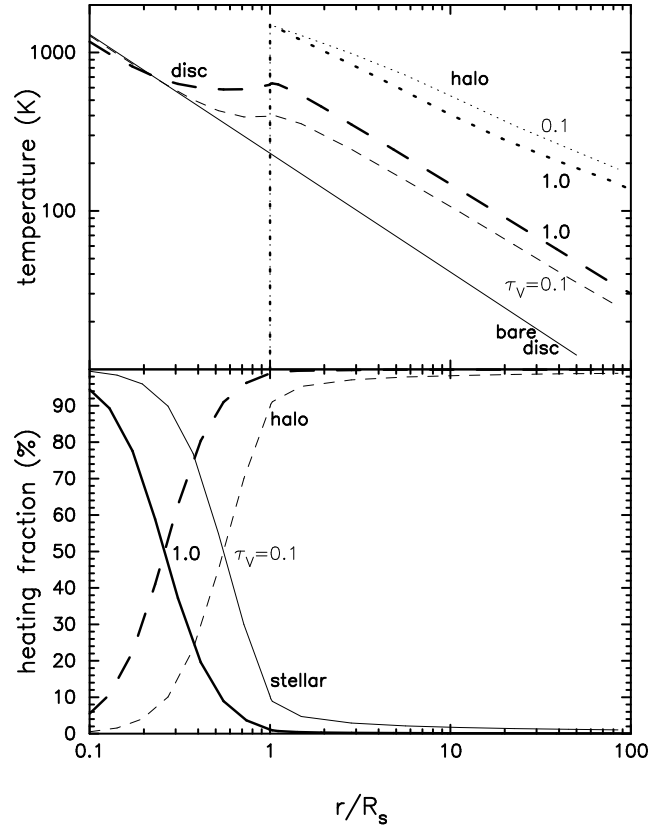


Figure 5. Top: Temperature profiles of a disk when heated only by a central star with $T_* = 10,000$ K (full line), and when imbedded in a spherical dusty halo with $\tau_V = 0.1$ or 1, as marked. The halo starts at dust sublimation $T_s = 1,500$ K and its density profile is $\propto r^{-2}$. The temperature profile of the halo is also shown in each case. Bottom: The fractional contributions of the halo and (attenuated) stellar components to heating of the disk

Our calculations confirm this important point. Figure 5 shows the temperature profile for a disk around a $T_* = 10,000$ K star when ‘‘bare’’ and when imbedded in a spherical halo with $\eta \propto y^{-2}$ and $\tau_V = 0.1$ and 1¹. Even though a halo with τ_V as small as 0.1 is almost transparent to the stellar radiation, it still causes a large rise in disk temperature. As is evident from the bottom panel, the halo contribution to the disk heating overtakes the stellar contribution inside the dust-free cavity and dominates completely once the dust is entered. Wolf et al (2003) present a similar figure for their model.

A dusty envelope with $\tau_V = 0.1$ intercepts only about 10% of the stellar luminosity while the disk intercepts 25% of that luminosity. So how can the halo dominate the disk heating? The reason is that direct heating of the disk by the star occurs predominantly at small radii. The disk absorbs more than 90% of its full stellar allotment within $10R_*$ while its entire remaining area, even though so much larger, absorbs only $0.025L$. From equation A1, the halo starts at $R_s \sim 100R_*$, where \mathcal{H}_* has already declined to $\sim 10^{-6}$ of its value at the stellar surface. In contrast, the halo emission is isotropic, therefore half of the radiation it intercepts is re-radiated

¹ The addition of a halo can only raise the disk temperature, yet figure 5 shows that our calculated profile for $\tau_V = 1$ dips slightly below that of the bare disk at $a \lesssim 0.2$. This happens because we neglect the disk emission in the calculation of the halo temperature. The error introduced by this approximation is of order 2% when $\tau_V = 1$, and even less at smaller τ_V .

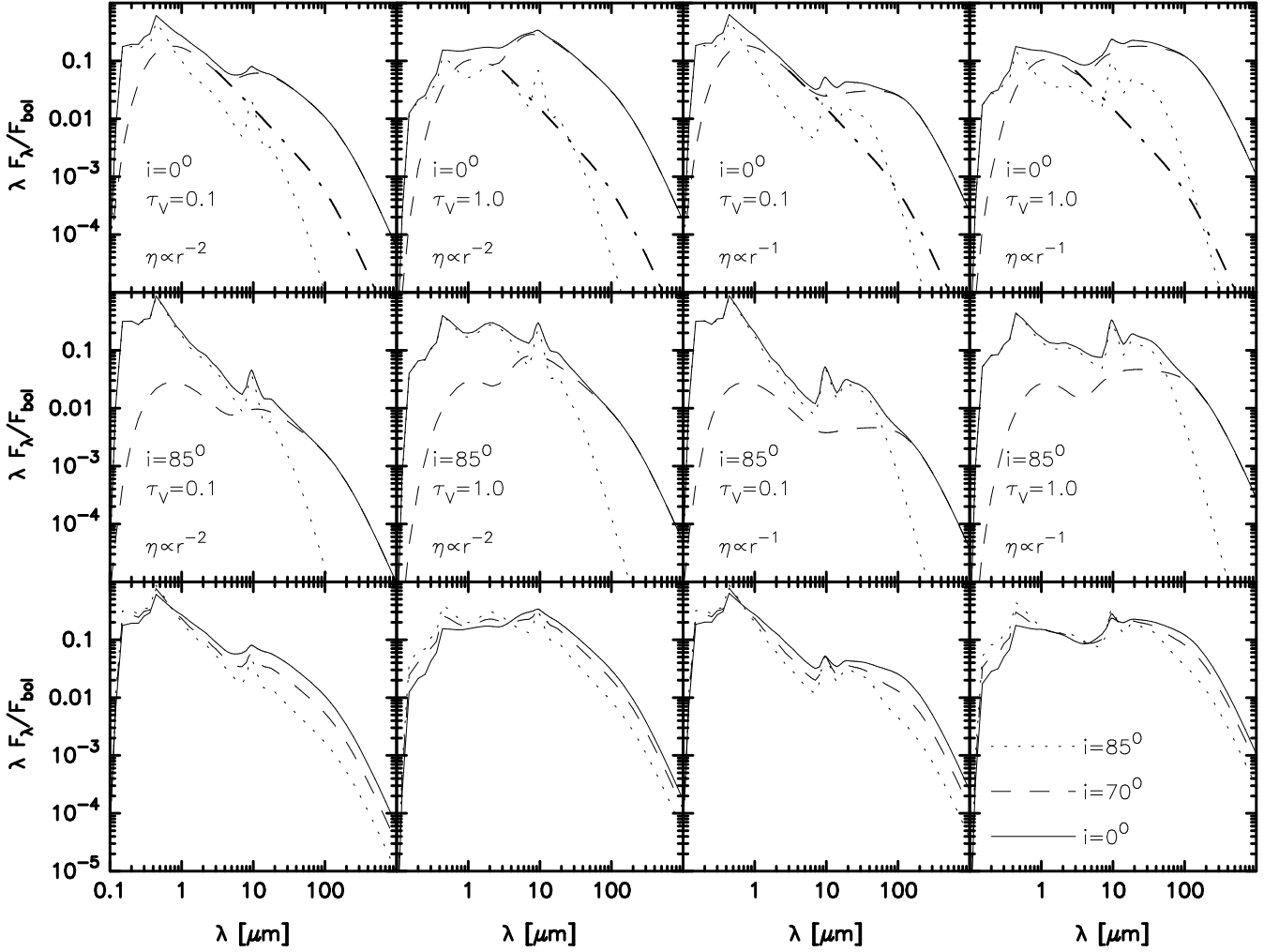


Figure 6. Sample SEDs for halo-imbedded-disks around stars with $T_* = 10,000$ K. The halo starts at R_s where $T_s = 1,500$ K and extends to $1,000R_s$, with density profile η and optical depth τ_V as indicated. The disk starts at the stellar surface and extends to the radius R_d set by the edge temperature $T_d = 25$ K (see Table 1). Each SED is normalized with the bolometric flux $F_{\text{bol}} = F(D, i)$ of the appropriate viewing angle (see equation 16). Top row: The SED for pole-on viewing. Full lines denote the overall flux, dotted lines the spherical (halo + attenuated stellar) component and dashed lines the disk component. The thick dot-dashed line is the flux from a face-on “bare” disk in the absence of an imbedding halo. It is omitted in the other rows. Mid row: Same models viewed at inclination angle $i = 85^\circ$. Bottom row: Variation of the overall SED with viewing angle i . Results for $i < 70^\circ$ are barely distinguishable from $i = 0^\circ$.

toward the disk, greatly exceeding the direct stellar contribution. Further insight can be gained from the approximate solution presented in Ivezic & Elitzur (1997; IE hereafter) for radiative transfer in spherical symmetry. From equations 20 and B4 of IE it follows that disk heating by a halo with $\tau_V \lesssim 1$ and $\eta \propto y^{-p}$ is roughly

$$\mathcal{H}_{\text{h}} = \frac{3F_s}{8} \frac{p-1}{p+1} \tau_V \times \begin{cases} 1 & a < 1 \\ 1/a^{1+p} & a > 1 \end{cases} \quad (18)$$

when $p > 1$; when $p = 1$ the factor $(p-1)/(p+1)$ is replaced by $1/(2 \ln Y)$. This yields $T \propto a^{-(1+p)/4}$, corroborating Natta’s result and extending its validity beyond the single-wavelength scattering approximation she employed. The temperature profile is similar to that of a bare disk when $p = 2$ but more moderate when $p < 2$. More importantly,

$$\left. \frac{\mathcal{H}_{\text{h}}}{\mathcal{H}_*} \right|_{a=1} = \frac{9\pi}{16} \frac{p-1}{p+1} \frac{R_s}{R_*} \tau_V. \quad (19)$$

And since $R_s \sim 100R_*$, the halo dominates the heating at $a = 1$ for τ_V as small as 0.02 when $p = 2$. As τ_V increases, the halo dominance of the heating moves inside the cavity. There the halo heating remains approximately constant while the stellar heating varies as a^{-3} , therefore stellar heating dominates only at $a \lesssim (60\tau_V)^{-1/3}$, at larger distances the halo takes over. This explains the results presented in the lower panel of figure 5 as well as figure 9 in Wolf et al (2003).

The figure also shows the temperature profile of the halo. This profile is largely independent of τ_V , varying roughly as $y^{-2/(4+n)}$ when the long-wavelength spectral shape of the dust absorption coefficient is $q_\nu \propto \nu^n$. The important property evident in the figure is that the disk is much cooler than the envelope at all radii at which both exist and can also contain cooler material in spite of being much smaller, with far reaching consequences for the system radiation.

	$\tau_V = 0.1$		$\tau_V = 1$	
	x	Y_d	x	Y_d
r^{-1}	0.43	190	1.33	400
r^{-2}	0.47	85	1.56	135

Table 1. Derived parameters for the models whose SEDs are presented in figure 6. The luminosity ratio of the components is $x = L_{\text{disk}}/L_{\text{sph}}$ and the disk radius is $R_d = Y_d R_s$, set from the requirement $T_d = 25$ K. A “bare” disk ($\tau_V = 0$) has $x = \frac{1}{3}$ and $Y_d = 18$.

3.2 SED

From equation 16, the fractional contribution of the disk to the overall bolometric flux is

$$\rho = \frac{F_{\text{disk}}}{F_{\text{disk}} + F_{\text{sph}}} = \frac{2x \cos i}{1 + 2x \cos i}. \quad (20)$$

Face-on orientation gives the maximal $\rho = 2x/(1 + 2x)$ and the standard “bare” disk, with $x = \frac{1}{3}$, has $\rho \leq \frac{2}{5}$. Introduce the normalized SED $f_\nu = F_\nu/\int F_\nu d\nu$, with similar, separate definitions for the disk and spherical components of the flux. Then

$$f_\nu = \rho f_{\nu,\text{disk}} + (1 - \rho) f_{\nu,\text{sph}} \quad (21)$$

Since the disk flux obeys $F_{\nu,\text{disk}}(i) = F_{\nu,\text{disk}}(0) \times \cos i$ for the range of parameters considered here, $f_{\nu,\text{disk}}$ is independent of the viewing angle i , and the entire i -dependence of the SED comes from the mixing factor ρ .

Figure 6 shows sample SEDs for some representative models. The halos extend from R_s to $1,000R_s$, with density profiles and overall optical depths as indicated. The behavior of SEDs for spherical shells was discussed in IE and since the halo emission is unaffected by the imbedded disk, the SEDs plotted in dashed lines need no further discussion. The disk, on the other hand, is strongly affected by the halo as is evident from contrasting each disk SED, plotted in long-dashed line, with what it would have been in the absence of a halo (dot-dashed line). The two curves are identical within the first bump around $1 \mu\text{m}$, caused by the stellar heating. In the absence of a halo, the disk SED drops from that peak as $\lambda F_\lambda \propto \lambda^{-4/3}$. However, halo heating of the outer regions of the disk generates the second broad bump of disk radiation, which is almost two orders of magnitude higher than the “bare” disk emission.

The halo heating effect is also evident from other disk properties. The disks in these models start at the stellar surface and extend to a radius R_d where the temperature is $T_d = 25$ K. In the absence of a halo, this temperature would be reached at $Y_d = R_d/R_s = 18$. As Table 1 shows, heating by even a tenuous halo with $\tau_V = 0.1$ pushes this radius out by almost factor 5 for the steep density profile r^{-2} and another factor of 2 for the flatter r^{-1} profile which spreads the heating further away from the star. The impact of halo heating increases with τ_V , pushing R_d further out still. Similarly, the disk luminosity, $xL/(1 + x)$, is only $0.25L$ in the absence of a halo but increases as the halo directs more radiation toward it to the point that it becomes $0.6L$ when $\tau_V = 1$.

Although it is more compact, the disk can become the stronger emitter at long wavelengths so that the overall SED is dominated by the halo at IR wavelengths and by the disk at sub-mm and mm wavelengths. This role reversal affects also the wavelength behavior of images. Figure 7 shows a series of images at various wavelengths for a sample model. At IR wavelengths the image is dominated by the halo, displaying the size variation discussed in appendix A. The $0.6 \mu\text{m}$ image is dominated by scattering, the $\lambda \geq$

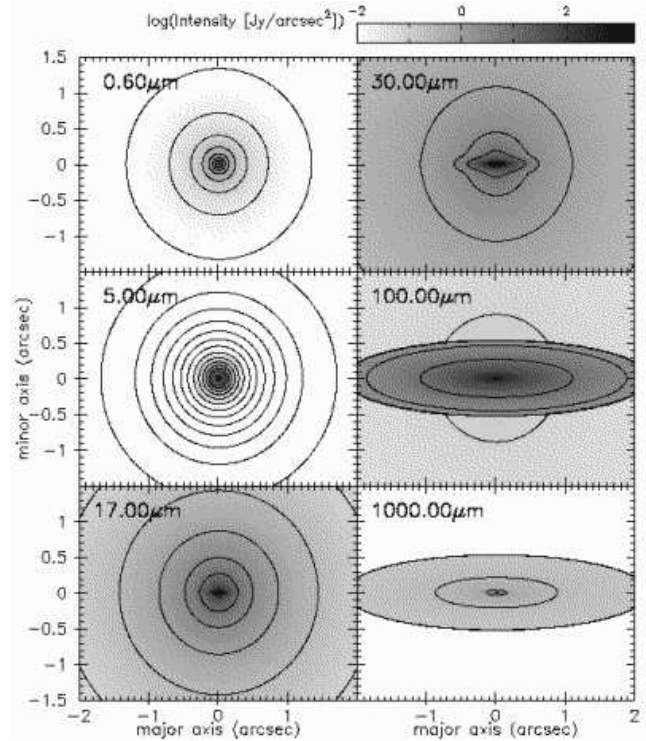


Figure 7. Images at various wavelengths of a halo-imbedded-disk around a star with $T_* = 10,000$ K. The halo starts at R_s where $T_s = 1,500$ K and extends to $1,000R_s$, with density profile $\eta \propto y^{-2} + 0.05y^{-1}$ and $\tau_V = 0.6$. The disk starts at the stellar surface and extends to radius R_d set by $T_d = 25$ K. The angular scale corresponds to bolometric flux $F_{\text{bol}} = 10^{-10} \text{ W m}^{-2}$. The viewing inclination angle is $i = 76^\circ$.

$5 \mu\text{m}$ images reflect dust emission, leading to size increase with wavelength. The disk emerges at $17 \mu\text{m}$ and dominates the $\lambda \geq 100 \mu\text{m}$ images. The finite beam size and dynamic range of any given telescope could result in an apparent size decrease between $10 \mu\text{m}$ and $100 \mu\text{m}$ in this case. Such an effect has indeed been discovered in the Haebes MWC 137, whose observed size decreases between $50 \mu\text{m}$ and $100 \mu\text{m}$ (DiFrancesco et al 1994, 1998). A switch from envelope to disk domination provides a simple explanation for this puzzling behavior. No single dust configuration can explain such a decrease, a conclusion reached already in MIVE and further affirmed by the results of appendix A. DiFrancesco et al (1998) suggest that this behavior might reflect multiple, rather than singular, sources of heating but the results of appendix A show the inadequacy of this conjecture. The region heated by any single source displays an increase of observed size with wavelength, and the superposition of multiple heating sources preserves this behavior. The opposite trend is possible only when the density distribution contains two distinct components, one optically thick, cool and compact, the other optically thin, warmer and more extended.

A similar effect was detected also in the dust-shrouded main-sequence star Vega. Van der Blik, Prusti & Waters (1994) find that its $60 \mu\text{m}$ size is $35'' \pm 5''$, yet $850 \mu\text{m}$ imaging by Holland et al. (1998) produced a size of only $24 \times 21'' \pm 3''$. So the dust distribution around Vega, too, could contain both spherical and disk components with the switch from halo- to disk-dominance occurring somewhere between 60 and $850 \mu\text{m}$. Indeed, imaging at 1.3 mm by Willner et al (2002) reveal the presence of the disk.

The calculation of the disk emission contains two free parameters, involving the temperature and optical depth at the disk edge.

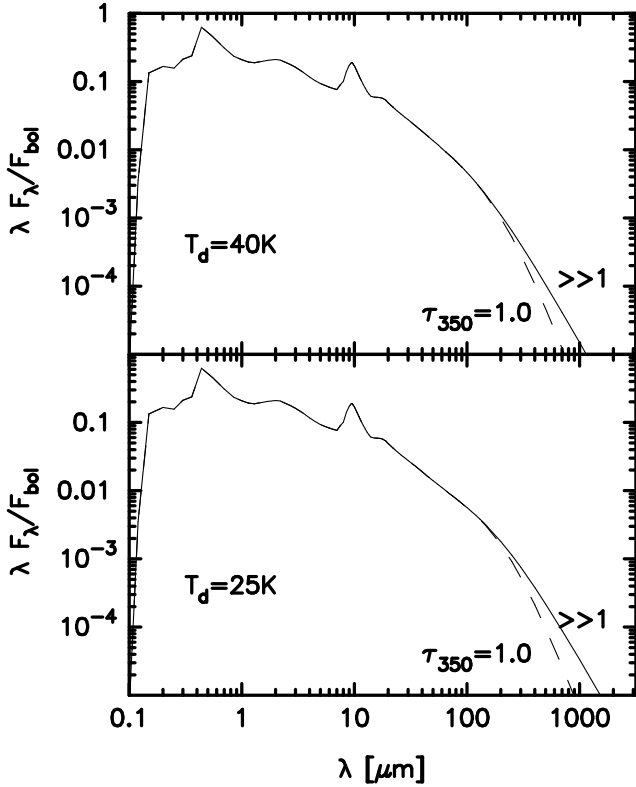


Figure 8. The effect on the SED of varying the temperature (T_d) and $350\mu\text{m}$ optical depth (τ_{350}) of the disk outer edge. The displayed model has $\tau_V = 0.5$ and $\eta \propto r^{-2}$. The viewing angle is 85° . Dashed lines correspond to $\tau_{350} = 1$, full lines to τ_{350} sufficiently large that the disk edge remains optically thick at all displayed wavelengths.

The disk outer radius R_d determines its lowest temperature T_d and a corresponding Planck-peak wavelength. While shorter wavelengths are emitted from a range of disk radii, all longer wavelengths originate from the edge of the disk. The resulting effect can be seen in figure 8, which shows two representative values of T_d . By the model assumptions the disk must be optically thick at the local Planck-peak wavelength everywhere, $\sim 350\mu\text{m}$ at $T_d = 25\text{K}$. As long as the disk edge remains optically thick also at longer wavelengths, the emission follows the Rayleigh-Jeans profile $f_{\nu,\text{disk}} \propto \nu^2$. Once the disk edge becomes optically thin, the SED switches to the steeper decline $f_{\nu,\text{disk}} \propto \nu^2 \sigma_\nu$ at longer wavelengths. The break in the disk SED is controlled by the optical depth of the disk edge, which we specify at $350\mu\text{m}$. Figure 8 shows also the effects of varying τ_{350} from its smallest value $\tau_{350} \sim 1$ to a value sufficiently large that the edge is optically thick at all the displayed wavelengths.

3.2.1 The disk inner radius

The bottom panel of each model in figure 6 shows the variation of the overall SED with viewing angle i . The entire variation comes from the mixing factor ρ (see equations 20 and 21). Since the parameters x and i enter only in the product $x \cos i$ but not separately, the SED is subject to a degeneracy: systems viewed at different inclination angles will have the same SED if they have the same $x \cos i$ in addition to all other properties. Because of the rapid decline with distance of the radiation absorbed from the star (cf eq. 17), the disk luminosity, i.e., x , has a steep dependence on its in-

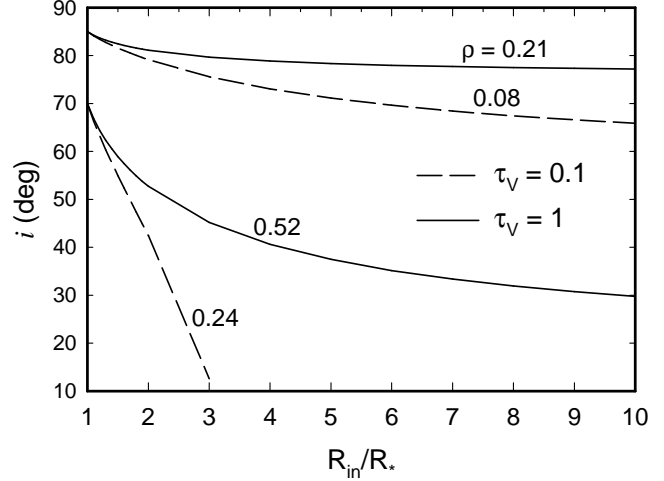


Figure 9. Contours of fixed mixing coefficient ρ (equation 20), as marked: The SEDs are the same as those presented in figure 6 for $i = 70^\circ$ and 85° when the disk inclination i and its inner radius R_{in} vary together along each of the plotted curves. The contours are virtually the same for the r^{-1} and r^{-2} halo density profiles.

ner radius R_{in} ; moving the disk inner edge from R_* to only $2R_*$ removes 56% of the stellar luminosity intercepted by the disk, $3R_*$ results in a 72% removal. Such central holes reduce x but do not impact any other relevant property because they remove only the hottest disk material whose contribution to the overall flux is negligible in comparison with the stellar component.

Figure 9 plots contours in the i - R_{in} plane of constant mixing factor ρ . It shows, for example, that the SEDs presented in figure 6 for $i = 70^\circ$ would be the same for systems viewed at $i = 35^\circ$ if the disk inner radius is increased from $1R_*$ to $2.2R_*$ in the $\tau_V = 0.1$ case and $6R_*$ for $\tau_V = 1$. Although the sizes of these holes cannot be determined from SED modeling of single stars, from statistical arguments MIVE conclude that their existence is essential to produce a plausible distribution of inclination angles.

3.2.2 Flared disks without halos

Thanks to the CG layer-halo equivalence, each model presented here describes also a disk with no halo and with the flaring angle defined by eq. 8 from η and τ_V . In particular, the SED presented for $\eta \propto 1/y^2$ halos describe also flared disks without halo and with $\alpha \propto 1/a$, those with $\eta \propto 1/y$ cover flared disks with constant grazing angle α ($\beta \sim \ln a$). The equivalence strictly holds only for disks and halos of the same size. However, the models presented would be little affected if each halo was truncated at R_d because that would only remove halo emission at long wavelengths where the SED is dominated by the disk anyhow. Since the flaring angle of each equivalent disk reaches $2\tau_V$ at its outer edge, halos whose optical depths require excessive flaring cannot be realized with disks only. This was the problem recognized by Stapelfeldt et al (2003) and Kikuchi et al (2002).

The equivalence holds only for the SED. High-resolution observations would produce widely different images for each halo and its equivalent flared disk, except when the latter is viewed face-on.

4 DISCUSSION

The results of §2.1 show that every disk imbedded in a halo with $\tau_V \lesssim \frac{1}{2}$ can be replaced by a flared disk without a halo and with an identical flux. This mathematical degeneracy explains the success of SED modeling with disk alone a system like GM Aur (Chiang & Goldreich 1999) even though the halo was subsequently discovered in imaging observations (Schneider et al 2003). It also explains why such modeling runs into difficulties and requires excessive flaring when the halos have larger τ_V , as is the case in HV Tau C (Stapelfeldt et al 2003) and flat-spectrum TTS in general (Kikuchi et al 2002).

Disks generally do not exist in pure vacuum. Equation 9 defines the circumstances under which the surrounding dust becomes the dominant component of the IR flux. Even at smaller τ_V , when not dominating the overall flux, the halo can still dominate the disk heating and make a strong impact on its temperature profile (§3.1). Ignoring the surrounding material can produce misleading results regarding the disk properties, such as its flaring profile.

In spite of the attractiveness of the flared disk as a simple, physical model without any additional components, imaging observations give irrefutable evidence for the existence of extended halos in pre main-sequence stars. The origin of these halos has not been studied yet. Stapelfeldt et al (2003) suggest that a replenishment process, either continued infall from the surrounding ISM or a dusty outflow from the source itself, is operating. It is noteworthy in this regard that accretion with the small rates of $\sim 10^{-8} M_\odot \text{ yr}^{-1}$ has been deduced from UV spectra of both Haebeles (Grady et al. 1996) and TTS (Valenti, Basri & Johns 1993; Gullbring et al 1998; Lamzin, Stempels & Piskunov 2001), and is consistent with halos that have $\tau_V \sim 0.1$ (MIVE). These low rates cannot correspond to the main accretion buildup of the star but rather a much later phase, involving small, residual accretion from the environment. The corresponding accretion luminosities are only $\sim 0.1 L_\odot$, justifying their neglect in our calculations.

In addition to the CG layer–halo equivalence, our results reveal numerous degeneracies that underscore the severe limitations of attempts to determine the dust morphology from SED analysis without imaging observations. The SED of a halo-imbedded-disk remains the same when the viewing angle and the size of the disk central hole vary together as shown in figure 9. From the results of appendix A, the SED of a spherical shell with power-law density profile $1/r^p$ displays a dependence on p only when $p \lesssim 2.6$, and then only in the spectral region $\lambda \leq \lambda_{\text{out}}$. All other regions of p and λ produce the same universal behavior $F_\nu \propto \nu^2 \sigma_\nu$ (§A4). The dust optical properties introduce additional degeneracies. The results of §A4 show that the frequency dependence of σ_ν and the radial dependence of the density profile can be interchanged on occasion without affecting the SED. The fundamental reason for all these degeneracies is that the flux from an optically thin source involves a volume integration (eq. A7) that tends to remove much of the dependence on the underlying morphology. Although the specific degeneracies we uncovered involve spherical geometry, the general analysis in appendix A shows that the spherical idealization is not essential. The dust distribution can be flattened and even distorted into irregular shape before severely affecting the results.

These degeneracies make it impossible to determine the geometry from a fit to the SED alone without additional input. Only imaging can trace the actual density distribution, and scattering provides a more faithful presentation because, unlike emission which involves also the dust temperature, it involves only the density distribution. Reliance on SED modeling alone can produce misleading

results, as was the case for the parameters of the flared disk in GM Aur.

ACKNOWLEDGMENTS

The partial support of NSF and NASA is gratefully acknowledged. Ž.I. acknowledges generous support by Princeton University.

REFERENCES

- Butner H.M., Natta A. & Evans N.J. II, 1994, ApJ, 420, 326
 Chiang, E.I. & Goldreich, P., 1997, ApJ, 490, 368 (CG)
 Chiang, E.I. & Goldreich, P., 1999, ApJ, 519, 279
 Chiang, E.I., et al 2001, ApJ, 547, 1077
 Creech-Eakman, M.J., Chiang, E.I., Joungh, R.M.K., Blake, G.A. & van Dishoeck, E.F., 2002, A&A, 385, 546
 D’Alessio, P., Calvet, N. & Hartmann, L. 1997, ApJ, 474, 397
 Di Francesco J., et al, 1994, ApJ, 432, 710
 Di Francesco J., et al, 1998, ApJ, 509, 324
 Dullemond, C.P., et al, 2001, ApJ, 560, 957
 Friedjung, M., 1985, A&A, 146, 366
 Grady C.A., et al., 1996, A&AS, 120, 157
 Grady, C.A., et al, 2001, AJ, 122, 3396
 Gullbring, E., Hartmann, L., Briceño, C. & Calvet, N., 1998, ApJ, 492, 323
 Harvey, P.M., Lester, D.F., Brock, D. & Joy, M., 1991, ApJ, 368, 558
 Hillenbrand, L. A., Strom, S. E., Vrba, F. J., & Keene, J. 1992, ApJ, 397, 613
 Holland, W.S. et al. 1998, Nature, 392, 788
 Ivezić Ž., Elitzur M., 1997, MNRAS, 287, 799 (IE)
 Ivezić Ž., Nenkova M. & Elitzur M., 1999, User Manual for DUSTY, Internal Report, University of Kentucky, accessible at <http://www.pa.uky.edu/~moshe/dusty/>
 Kenyon S.J., Hartmann L. 1987, ApJ, 323, 714
 Kikuchi, N., Nakamoto, T., & Ogochi, K. 2002, PASJ, 54, 589
 Kurucz R.L., 1994, CD-ROM No.19, Smithsonian Astrophys. Observ.
 Lamzin, S.A., Stempels, H.C. & Piskunov, N.E., 2001, A&A, 369, 965
 Miroshnichenko, A.S., Ivezić, Ž., Vinković, D. & Elitzur, M., 1999, ApJ, 520, L115 (MIVE)
 Natta, A. 1993, ApJ, 412, 761
 Natta, A. et al., 2001, A&A, 371, 186
 Polomski, E.F., Telesco, C.M., Piña, R., & Schulz, B., 2002, AJ, 124, 2207
 Schneider, G., et al, 2003, AJ, 125, 1467
 Stapelfeldt, K.R., et al, 2003, ApJ, 589, 410
 Valenti, J.A., Basri, G. & Johns, C.M. 1993, AJ, 106, 2024
 van der Blik, N.S., Prusti, T. & Waters, L.B.F.M. 1994, A&A, 285, 229
 Whitney, B.A. & Hartmann, L., 1992, ApJ, 395, 529
 Willner, D.J., Holman, M.J., Kuchner, M.J. & Ho, P.T.P., 2002, ApJ, 569, L115
 Wolf, S., Padgett, D.L., & Stapelfeldt, K.R., 2003, ApJ, 588, 373
 Wood, K., Kenyon, S.J., Whitney, B. & Turnbull, M.W., 1998, ApJ, 497, 404

APPENDIX A: OPTICALLY THIN DUST

Consider a cloud heated from inside by a star of radius R_\star and effective temperature T_\star (figure A1). The star clears out a dust-free cavity of radius R_s , determined by dust sublimation $T(R_s) = T_s$. When the dust is optically thin, the cavity radius can be found from

$$\frac{R_s}{R_\star} = \frac{1}{2} \left(\frac{\bar{\sigma}(T_\star)}{\bar{\sigma}(T_s)} \right)^{1/2} \left(\frac{T_\star}{T_s} \right)^2 \quad (\text{A1})$$

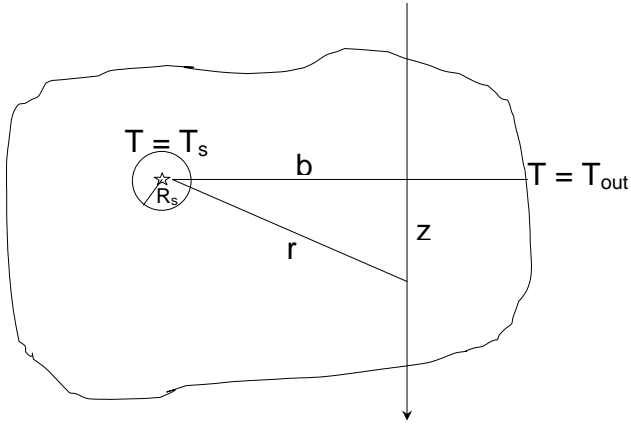


Figure A1. A star imbedded in a cloud clears out a dust-free cavity of radius R_s , corresponding to dust sublimation temperature T_s (equation A1). The dust temperature declines with radial distance toward its surface value T_{out} . The intensity at impact parameter b is obtained from integration along the indicated path toward the observer.

where $\bar{\sigma}(T)$ is the Planck average at temperature T of the absorption cross section σ_ν (IE). With standard interstellar dust and $T_s = 1500$ K, the cavity radius obeys $R_s/R_\star \simeq 100$ at a typical Haebes temperature $T_\star = 10,000$ K. In TTS, on the other hand, the dust is much closer to the star: R_s/R_\star is only 15 at $T_\star = 5,000$ K and as small as 3 at $T_\star = 3,000$ K. The intensity at frequency ν and impact parameter b (fig. A1) is

$$I_\nu(b) = \sigma_\nu \int [(1 - \varpi_\nu)B_\nu + \varpi_\nu J_\nu] n_d dz, \quad (\text{A2})$$

assuming isotropic scattering. Here n_d is the dust density, z is distance along the path to the observer, ϖ_ν is the albedo at frequency ν and $J_\nu = \int I_\nu d\Omega/4\pi$. This expression neglects self-absorption by the dust; the error in this approximation is of order $1 - \exp(-\int \sigma_\nu n_d dz)$.

A1 Scattering Wavelengths

Since the dust temperature cannot exceed the sublimation temperature T_s , there is no dust emission at $\lambda \lesssim 4\mu\text{m} \times (1000\text{K})/T_s$, only scattering. Diffuse radiation and attenuation between the star and the scattering point can be neglected since our discussion is centered on optically thin dust. Then the only source of scattering is the stellar radiation with energy density $J_\nu = L_\nu/4\pi r^2$, where L_ν is the stellar luminosity at frequency ν . From equation A2, the scattered brightness is

$$I_\nu(\theta) = \frac{L_\nu}{4\pi} \varpi_\nu \sigma_\nu \int \frac{n_d dz}{r^2}, \quad (\text{A3})$$

where $\theta = b/D$ and D is the distance to the observer. Since the frequency- and geometry-dependence separate out, all scattering wavelengths share a common image. Only the brightness level varies with ν , and because of the wavelength decline of $\varpi_\nu \sigma_\nu$ the observed size generally *decreases with wavelength* when traced to the same brightness level. In any geometry the scattering image always traces directly the variation of column density along the line of sight, the dust temperature profile is irrelevant.

A2 Emission Wavelengths

At wavelengths longer than $\sim 3\mu\text{m}$, $\varpi_\nu < 10^{-2}$ and scattering can be neglected. The Planckian enters in equation A2 as a function of T at fixed ν , which can be well approximated by its Rayleigh-Jeans limit at $T \geq T_\nu = 0.56h\nu/k$ and a sharp cutoff at T_ν . With this approximation the integration is limited to locations along the path where $T \geq T_\nu$; regions with $T < T_\nu$ are too cold to emit appreciably at frequency ν . Excluding highly patchy geometries, the highest temperature on the path occurs at $r = b$ (i.e., $z = 0$), the closest distance to the star, and only paths with $T(b) > T_\nu$ contribute to the brightness. As z increases in either direction, T decreases. The integration is truncated either because the temperature becomes too low, in which case the emission is *temperature bounded*, or because the edge of the source is reached and the emission is *matter bounded*. Denote the resulting integration limits Z_i ($i = 1, 2$), then

$$I_\nu(\theta) = \frac{2}{c^2} \nu^2 \sigma_\nu \int_{Z_1}^{Z_2} kT n_d dz. \quad (\text{A4})$$

In the matter bounded case Z_i is the edge of the source, the integral is independent of ν and the frequency dependence of the intensity follows $\nu^2 \sigma_\nu$. In the case of temperature bounded emission the integration limits introduce additional ν -dependencies that modify this behavior. However, the integration can be extended to ∞ whenever (1) $Z_i \gg b$ and (2) the product $n_d T$ of dust density and temperature declines along the path faster than $1/z$. Therefore, *when these two conditions are met, the frequency variation of optically thin emission is $I_\nu \propto \nu^2 \sigma_\nu$ even when it is temperature bounded*. Independent of geometry, all frequencies that obey these conditions produce a common image, similar to the scattering case; only the scale of brightness varies with ν . This result makes it possible to determine the wavelength dependence of the dust cross section directly from imaging observations.

Similar to the variation along the line of sight, when b increases (moving away from the star) the emission again is truncated by either the matter or temperature distribution. Denote by T_{out} the temperature at the source outer edge. The corresponding emission cutoff wavelength is

$$\lambda_{\text{out}} = 100\mu\text{m} \times \frac{40\text{K}}{T_{\text{out}}}. \quad (\text{A5})$$

When $\lambda > \lambda_{\text{out}}$, the dust is sufficiently warm everywhere that the emission is truncated only by the matter distribution. The observed size is then Θ , the angular displacement of the source edge from the star, the same for all wavelengths. However, when $\lambda < \lambda_{\text{out}}$ the brightness is truncated when $T(b) \leq T_\nu$ before the edge of the source is reached, resulting in a wavelength-dependent angular size $\theta_\lambda < \Theta$. The observed size of optically thin emission *increases with wavelength* so long as $\lambda < \lambda_{\text{out}}$, the opposite of the trend at scattering wavelengths.

The frequency variation of the dust cross section is well described by $\sigma_\nu \propto \nu^n$ with $n = 1-2$. Then to a good degree of approximation, the temperature variation of optically thin dust is $T \propto 1/r^t$, where $t = 2/(4+n)$, producing the wavelength-dependent observed angular size

$$\theta_\lambda = \Theta \times \begin{cases} \left(\frac{\lambda}{\lambda_{\text{out}}}\right)^{1/t} & \lambda < \lambda_{\text{out}} \\ 1 & \lambda \geq \lambda_{\text{out}} \end{cases} \quad (\text{A6})$$

Since $t < \frac{1}{2}$, θ_λ increases faster than λ^2 , a fairly steep rise.

A3 Flux—the SED

The flux can be obtained from equation A2 by integration over the observed area. At emission wavelengths, the flux at distance D is

$$F_\nu = \frac{\sigma_\nu}{D^2} \int B_\nu(T) n_d dV. \quad (\text{A7})$$

Since the temperature profile of optically thin dust depends only on distance from the star, the dependence on the source geometry enters only from n_d .

As before, the integration is truncated by either the temperature or the matter distribution. Whenever $\lambda > \lambda_{\text{out}}$ at every point on the surface, the emission is matter bounded everywhere and the integration encompasses the entire source. Under this circumstances $F_\nu \propto \nu^2 \sigma_\nu$, a universal SED that depends only on the dust properties irrespective of geometry. In particular, the spectral variation $\sigma_\nu \propto \nu^n$ gives $F_\nu \propto \nu^{2+n}$, therefore the signature of matter bounded emission is this SED accompanied by wavelength independent images; this is the expected behavior in any geometry at sufficiently long wavelengths. At $\lambda < \lambda_{\text{out}}$ the integration volume is truncated by the temperature, and since the emission volume decreases as the frequency increases, the rise of F_ν with ν becomes less steep than in the matter dominated regime. Therefore, the SED changes from $F_\nu \propto \nu^{2+n}$ at $\lambda > \lambda_{\text{out}}$ to a flatter slope at $\lambda < \lambda_{\text{out}}$.

The break in the slope at λ_{out} can be used to determine the surface temperature T_{out} . Flux spectral variation shallower than ν^3 is a clear indication of temperature-bounded emission and should be accompanied by an image size that increases with wavelength.

A4 Spherical Geometry

Some explicit results are easily derived in the case of spherical symmetry. Thanks to the scaling properties of dust radiative transfer (IE), only two properties are required to specify the geometry. The first is the radial optical depth at one wavelength, say $\tau_\nu = \sigma_\nu \int n_d dr$ where σ_ν is the cross-section at visual; at every other wavelength, $\tau_\nu = q_\nu \tau_V$ where $q_\nu = \sigma_\nu / \sigma_V$. The second is the dimensionless, normalized profile of the dust density distribution

$$\eta(y) = \frac{n_d(y)}{\int_1^\infty n_d dy} \quad (\text{A8})$$

where $y = r/R_s$; note that $\int \eta dy = 1$. Explicit results follow immediately for all power-law density profiles where

$$\eta = \frac{\mathcal{N}}{y^p} \quad \mathcal{N} = \begin{cases} (p-1)/(1-Y^{1-p}) & p \neq 1 \\ (\ln Y)^{-1} & p = 1 \end{cases} \quad (\text{A9})$$

The shell extends to the outer radius $Y R_s$, subtending the angular region $\theta_s \leq \theta \leq \Theta$, where $\theta_s = R_s/D$ and $\Theta = Y\theta_s$. At scattering wavelengths

$$I_{\nu, \text{sca}}(\theta) = \frac{\mathcal{N}}{2\pi} \tau_V L_\nu \varpi_\nu q_\nu \left(\frac{\theta_s}{\theta}\right)^{p+1} \times \int_0^{\sqrt{(\Theta/\theta)^2-1}} \frac{du}{(1+u^2)^{(p+2)/2}} \quad (\text{A10})$$

Whenever $\theta \ll \Theta$ the integration can be extended to ∞ , yielding $I(\theta) \propto 1/\theta^{p+1}$; the brightness decreases as a power law so long as the observation direction is not too close to the halo edge. At emission wavelengths, on the other hand,

$$I_{\nu, \text{em}}(\theta) = \frac{4\mathcal{N}}{c^2} k T_s \tau_V \nu^2 q_\nu \left(\frac{\theta_s}{\theta}\right)^{p+t-1} \times \int_0^{\sqrt{(\theta_\lambda/\theta)^2-1}} \frac{du}{(1+u^2)^{(p+t)/2}} \quad (\text{A11})$$

where the observed size θ_λ is smaller than Θ when $\lambda < \lambda_{\text{out}}$ (equation A6). As long as $\theta \ll \theta_\lambda$ the integration can be extended to ∞ and the brightness then decreases along any radial direction in proportion to $1/\theta^{p+t-1}$.

The flux integration in equation A7 is similarly terminated at the observed boundary θ_λ , producing

$$F_\nu = \frac{8\pi\mathcal{N}}{c^2} k T_s \theta_s^2 \tau_V \frac{\nu^2 q_\nu}{3-(p+t)} \left[\left(\frac{\theta_\lambda}{\theta_s}\right)^{3-(p+t)} - 1 \right]. \quad (\text{A12})$$

Since $\theta_\lambda > \theta_s$, there are two families of SED. In the case of steep density distributions with $p > 3-t$, the first term inside the brackets can be omitted because $3-(p+t) < 0$. Such distributions produce $F_\nu \propto \nu^2 \sigma_\nu$ irrespective of the actual value of p . Since typically $t \sim 0.4$, this behavior applies to all cases of $p \gtrsim 2.6$. On the other hand, whenever $p < 3-t$ the omitted term dominates and the SED is a broken power law. The power index switches from the universal $2+n$ at $\lambda \geq \lambda_{\text{out}}$ to the geometry-dependent value $3+n-(3-p)/t$ (see also Harvey et al 1991) at $\lambda \leq \lambda_{\text{out}}$.

These results show that the SED displays a dependence on the density profile only when $p \lesssim 2.6$, and then only in the spectral region $\lambda \leq \lambda_{\text{out}}$. All other regions of p and λ produce the universal behavior $F_\nu \propto \nu^2 \sigma_\nu$.